# Multifrequency InSAR Canopy Height Improves Generalization of Savanna Biomass Models

Preet Lal, John Armston, Narayanarao Bhogapurapu, *Member, IEEE*, Mikhail Urbazaev, Paul Siqueira, *Senior Member, IEEE*, Konrad J. Wessels, Ralph Dubayah, and Laura Duncanson

***Abstract*—The aboveground biomass (AGB) estimation in savanna ecosystems remains challenging due to structural heterogeneity and phenological dynamics of woody vegetation. This study developed two physically based models integrating multifrequency synthetic aperture radar (SAR) observations from ALOS-2 PALSAR-2 (L-band) and Sentinel-1 (C-band) over Kruger National Park (KNP), South Africa, and the Injune Landscape Collaborative Project (ILCP), Australia. The additive saturation model combines backscatter and interferometric coherence as independent exponential terms, while the hybrid allometric-backscatter model integrates canopy height derived from random volume over ground (RVoG) inversion with unified backscatter. Under site-specific calibration, both models achieved comparable accuracy ($R^2$ = 0.63–0.65). Under combined calibration, the additive model degraded ($R^2$ = 0.612, root mean square error (RMSE) = 19.77 Mg ha$^{-1}$, concordance correlation coefficient (CCC) = 0.756 because independent saturation terms could not adapt to site-dependent scattering mechanisms. The hybrid model maintained stronger performance under combined calibration ($R^2$ = 0.731, RMSE = 16.35 Mg ha$^{-1}$, and CCC = 0.841). The Shapley sensitivity analysis revealed that L-band backscatter dominated under site-specific calibration ($\phi$ = 0.74–0.83), while RVoG-derived C-band height metrics became the primary contributor under combined calibration at 40–80 Mg ha$^{-1}$, where backscatter sensitivity diminishes. The allometric height–AGB relationship follows fundamental growth principles consistent across the pooled AGB gradient, supporting the robustness of the hybrid model under multisite calibration.**

***Index Terms*—Aboveground biomass (AGB), backscatter, coherence, GEDI, savannas.**

## I. Introduction

SAVANNA ecosystems cover approximately 20% of Earth's terrestrial surface and contribute 25%–30% of global net primary production [1]. African savannas represent a critical yet poorly quantified carbon stock, largely due to the challenges of assessing open-canopy and heterogeneous vegetation structure [2]. Accurate aboveground biomass (AGB) monitoring in savannas is essential for rangeland management, climate mitigation initiatives [3], and national carbon accounting systems. These ecosystems present distinct challenges for AGB estimation, with their highly heterogeneous vertical structure, high spatial variability [4], [5], as well as pronounced seasonality and variable moisture conditions [6]. Airborne lidar directly measures 3-D canopy structure, supporting accurate estimation of AGB [7], [8]. However, airborne and satellite lidar are spatially constrained to a sample of Earth's land surface and alone cannot provide the repeated and spatially complete global acquisitions required for large-area biomass monitoring. The synthetic aperture radar (SAR) offers distinct advantages for AGB estimation [9]. Depending on wavelength, polarization, and incidence angle, the microwaves penetrate the canopy, interact with canopy scatterers, and subsequently create a volume scattering response. However, the standard backscatter-based (radar cross section) retrieval faces two compounding limitations [10], [11]. First, backscatter saturation limits sensitivity at higher biomass levels (>70 Mg/ha) despite using longer wavelengths [12]. Second, surface and soil moisture strongly modulate backscatter in open canopies [4], [6]. Variations in the soil dielectric constant introduce a moisture-dependent ground contribution that confounds the vegetation signal. This effect is most acute at low to moderate AGB, where canopy cover is sparse and microwaves reach the ground more easily, yielding a low vegetation signal-to-noise ratio [6]. The saturation and moisture constraints limit the wider applicability of backscatter-only approaches, necessitating alternative observables to retain sensitivity across the full AGB range and variable moisture conditions.

Interferometric SAR (InSAR) coherence provides a pathway to address this limitation through phase correlation between image pairs [13]. The coherence magnitude responds to volume scattering via temporal and volumetric decorrelation mechanisms within the canopy [14]. Unlike backscatter, coherence decreases with increasing vegetation density, retaining sensitivity in moderate- to high-AGB environments where backscatter saturates [15]. Studies in boreal forests have confirmed that coherence, under stable environmental conditions, is less affected by soil moisture than backscatter [16]. Multifrequency coherence further exploits wavelength-dependent penetration: C-band coherence reflects surface vegetation dynamics, while L-band coherence captures deeper woody structure [17]. However, using repeat-pass coherence alone faces challenges from temporal decorrelation caused by wind, moisture variations, and phenology. To address this limitation,

Received 14 April 2026; revised 2 July 2026; accepted 27 July 2026. Date of publication 31 July 2026; date of current version 14 August 2026. This work was supported by National Aeronautics and Space Administration (NASA) Carbon Monitoring System (United States) under Grant 80NSSC21K0967. *(Corresponding author: John Armston.)*

Preet Lal, John Armston, Ralph Dubayah, and Laura Duncanson are with the Department of Geographical Sciences, University of Maryland, College Park, MD 20742 USA (e-mail: armston@umd.edu).

Narayanarao Bhogapurapu is with the Department of Civil Engineering, National Institute of Technology Warangal, Warangal, Telangana 506004, India, and also with the Microwave Remote Sensing Laboratory (MiRSL), University of Massachusetts Amherst, Amherst, MA 01003 USA.

Mikhail Urbazaev is with GFZ Helmholtz Centre for Geosciences, 14473 Potsdam, Germany, and also with the Department of Geographical Sciences, University of Maryland, College Park, MD 20742 USA.

Paul Siqueira is with the Microwave Remote Sensing Laboratory (MiRSL), University of Massachusetts, Amherst, MA 01003 USA.

Konrad J. Wessels is with the Department of Geography and Geoinformation Science, George Mason University, Fairfax, VA 22030 USA.

Digital Object Identifier 10.1109/LGRS.2026.3718772

canopy height derived from interferometric coherence through the random volume over ground (RVoG) framework provides a more direct measure of structure [18], [19]. Height serves as an allometric proxy for AGB, providing biophysical information that improves biomass estimation and extends the dynamic range beyond backscatter saturation thresholds [20]. Since height inversion relies on interferometric phase rather than on intensity, it provides a structural observable that is less sensitive to the environmental conditions that bias backscatter-based estimates [21]. Studies combining L-band backscatter with InSAR-derived height have reported substantial accuracy improvements over backscatter-only models [21], [22].

The SAR-based AGB estimation in savannas has relied predominantly on backscatter-only approaches [4], [23], [24] or coherence used as a direct inverse proxy [15]. Integration of multifrequency backscatter with InSAR-derived canopy height has been explored in boreal and closed-canopy forests [21], [22]. Open savannas present a fundamentally different scattering regime. Double-bounce between woody trunks and ground often dominates and preserves coherence at high AGB, unlike closed-canopy forests where volume decorrelation causes coherence to decrease with biomass. The existing models do not account for this distinction. This study developed and evaluated two physically based models whose backscatter terms adopt an exponential saturation form $1 - e^{-\beta x}$ consistent with the vegetation contribution in the WCM [23], integrating multifrequency SAR backscatter, InSAR coherence, and RVoG-derived canopy height that was retrieved via sinc-based inversion of the coherence [18]: 1) an additive model that considers backscatter and coherence as independent saturation terms and 2) a hybrid model that integrates canopy height with backscatter. To evaluate model robustness across structurally diverse conditions, the algorithms were calibrated and validated across two contrasting savanna ecosystems. The first, Kruger National Park (KNP), South Africa, is a short, open savanna woodland and shrubland with low-to-moderate AGB. The second, Injune Landscape Collaborative Project (ILCP), Queensland, Australia, represents a taller savanna woodland with substantially higher AGB. The site-specific and combined calibration strategies were used to assess model robustness across these two structurally diverse ecosystems. Finally, a Shapley sensitivity analysis was used to quantify the contribution of each observable across AGB gradients, identifying predictor importance and its variation with biomass level.

## II. Study Areas and Datasets

Together, KNP in South Africa and the ILCP in Queensland, Australia, represent savanna ecosystems with continuous gradients in vegetation structure from shrublands to open forests. The KNP is comprised of Zambesian Mopane Woodlands, Central Bushveld, and Limpopo Lowveld ecoregions, while the ILCP site includes the Brigalow belt biogeographic region ("Brigalow Tropical Savanna"; [25], [26]). KNP is semi-arid, with a mean annual rainfall of 350–723 mm, hot wet summers (mean 26 °C), and mild dry winters (mean 9 °C); woody cover is sparse (<20%) and canopy heights are predominantly below 7 m [5], supporting low AGB (0–50 Mg ha$^{-1}$). ILCP operates under subhumid conditions with a mean annual rainfall of approximately 635 mm; vegetation comprises eucalypt and acacia woodlands with a canopy cover of 10%–60% [6] and higher AGB (40–150 Mg ha$^{-1}$). This structural contrast spanning open shrubland to dense woodland makes the two sites suitable for evaluating algorithm robustness across a wide range of savanna conditions.

TABLE I

Summary of Datasets Used in This Study

| Site | Dataset / Mode | Acquisition Period |
|---|---|---|
| KNP | ALS<br>Sentinel-1 (IW)<br>ALOS-2 PALSAR-2 (FBD) | Mar–Jun 2018<br>7 Aug and 19 Aug 2018<br>12 Aug and 21 Oct 2018 |
| ILCP | ALS<br>Sentinel-1 (IW)<br>ALOS-2 PALSAR-2 (FBD) | Aug 2015<br>22 Aug and 3 Sep 2018<br>27 Aug and 5 Nov 2018 |

IW = Interferometric Wide; FBD = Fine Beam Dual. SAR acquisitions were selected during the dry season (May–October) at both sites to minimize soil moisture variability; the second ALOS-2 acquisition extended into the seasonal transition due to the 70-day repeat cycle constraint.

Airborne lidar data and field plots provided reference AGB measurements for model calibration and validation. For KNP, individual tree AGB was derived from field-measured stem diameter and height using the Colgan et al.'s [27] allometric model, aggregated to 25 × 25 m plot level, and linked to ALS-derived mean canopy height and canopy cover grids [7]. For ILCP, the 25 × 25 m field plot AGB estimates (n = 44) were derived using the Paul et al.'s [28] allometric models and linked to ALS-derived relative canopy height metric grids [8]. The parametric regression models were trained following the GEDI Level-4A AGB model building framework [8], [29] and applied to the ALS-derived predictor grids to derive a 25-m reference AGB map.

Multifrequency SAR observations were obtained from Sentinel-1 (C-band) and ALOS-2 PALSAR-2 (L-band). Sentinel-1 data were acquired in interferometric wide (IW) mode with dual polarization (VV + VH) and 12-day temporal baseline. ALOS-2 PALSAR-2 data were obtained in fine beam dual (FBD) mode with dual polarization (HH + HV), with an approximately 70-day temporal baseline. Only the cross-polarized channels (VH for Sentinel-1 and HV for ALOS-2) were selected for analysis due to their enhanced sensitivity to vegetation volume scattering compared to co-polarized returns [23], [30].

## III. Methodology

The AGB estimation from SAR data exploits the sensitivity of microwave signals to canopy dielectric and structural properties. Backscatter intensity ($\sigma^0$) responds to moisture content and scattering strength, while InSAR coherence ($\gamma$) captures vertical structure through decorrelation mechanisms [18] [note that throughout this study, terrain-flattened backscatter ($\gamma^0$) is used; $\sigma^0$ is adopted here solely for notational clarity]. These observables exhibit complementary sensitivities: backscatter saturates at moderate AGB due to signal attenuation, whereas coherence-derived height metrics maintain sensitivity through allometric scaling relationships. To exploit this complementarity, two retrieval frameworks are developed: 1) an additive model and 2) a hybrid model.

### A. Additive Saturation Model

The additive exponential saturation model represents AGB as the superposition of independent contributions from multifrequency SAR observables. Each observable is expressed through an exponential saturation function of the form $1 - e^{-\beta x}$, capturing high sensitivity at low AGB and asymptotic response where signal saturation occurs. The predicted AGB is formulated as

$$\begin{aligned}\mathrm{AGB} = \; & a_1\left(1 - \mathrm{e}^{-|b_1|\sigma_L}\right) + a_2\left(1 - \mathrm{e}^{-|b_2|\sigma_C}\right) \\ & + a_3\left(1 - \mathrm{e}^{-|c_1|\gamma_L}\right) + a_4\left(1 - \mathrm{e}^{-|c_2|\gamma_C}\right) + a_5 \qquad (1)\end{aligned}$$

where $\sigma_L$ and $\sigma_C$ denote the L-band and C-band HV backscatter coefficients, respectively, and $\gamma_L$ and $\gamma_C$ represent the interferometric coherence magnitudes. The coefficients $a_1$–$a_4$ define asymptotic saturation limits, while $b_1$, $b_2$, $c_1$, and $c_2$ control saturation rates and $a_5$ accounts for calibration offset. The model satisfies monotonicity under $a_1$–$a_4 \geq 0$, ensuring AGB increases with all observables. In open savannas, backscatter at high AGB is typically dominated by double-bounce scattering between woody trunks and the ground [31] and preserves InSAR coherence between acquisitions. Conversely, soil moisture variability over exposed bare soil in low-AGB areas reduces coherence [32]. This behavior is distinct from the inverse relationship typically observed in closed-canopy forests, where volume decorrelation dominates.

### B. Hybrid Allometric-Backscatter Model

InSAR coherence encodes vertical structure that can be inverted to retrieve canopy height using the RVoG model with sinc-based inversion [18]. While coherence-derived height captures structural information, it does not account for radiometric sensitivity to canopy density. Conversely, backscatter alone saturates at moderate AGB levels. In the context of this study, the low, moderate, and high AGB refer to the ranges of 0–20, 20–60, and >60 Mg ha$^{-1}$, respectively. The hybrid formulation overcomes these limitations by integrating L-band and C-band height metrics ($H_L$, $H_C$) through power-law scaling, while modeling combined backscatter with a unified exponential saturation term. Since microwave penetration depth increases with wavelength, $H_L$ and $H_C$ carry complementary structural information, with the calibrated exponents $b$ and $f$ weighting their respective contributions to AGB implicitly

$$\mathrm{AGB} = a\,H_L^b + e\,H_C^f + c\left(1 - \mathrm{e}^{-|d|(\sigma_L+\sigma_C)}\right) + g \qquad (2)$$

where $a$ and $e$ are the scaling coefficients converting height to AGB units, $b$ and $f$ are the allometric exponents controlling the height-AGB curvature, $c$ defines the asymptotic backscatter saturation limit, $d$ regulates the saturation rate, and $g$ accounts for calibration offset. The power-law formulation captures the established allometric principles governing AGB accumulation, where tree height scales with stem volume and woody mass.

The model satisfies monotonicity constraints under $a, e, c \geq 0$ and $b, f > 0$, ensuring AGB increases with all observables. All partial derivatives remain nonnegative, ensuring biologically realistic responses across all observable ranges. In the low-AGB regime, the exponential term approximates linear behavior as $c|d|(\sigma_L+\sigma_C)$, while height contributions approach zero as $H \rightarrow 0^+$. In the high-AGB regime, backscatter saturates asymptotically to $c$, whereas height terms continue increasing at rates determined by their allometric exponents.

### C. Parameter Estimation and Validation

Both the additive saturation model and hybrid allometric-backscatter model were calibrated using ALS-derived AGB as reference. To ensure spatial consistency and reduce SAR speckle, all inputs, including backscatter coefficients, InSAR coherence, RVoG-derived canopy heights, and reference AGB, were spatially aggregated to a common 100-m UTM grid, ensuring pixel alignment across all datasets. The model parameters were estimated using nonlinear least squares optimization under two calibration strategies: 1) combined calibration pooling data from KNP and ILCP to derive generalized parameters and 2) site-specific calibration capturing local scattering behavior. For validation, 40% of observations were withheld using stratified random sampling to preserve the AGB distribution. Random holdout assumes spatially uncorrelated errors, which may inflate reported accuracy statistics. However, as this assumption is applied consistently across all model configurations and calibration strategies, relative comparisons between models remain valid. Performance was quantified using the coefficient of determination ($R^2$), root mean square error (RMSE), mean bias, and concordance correlation coefficient (CCC).

### D. Sensitivity Analysis

The Shapley effects were computed to quantify the relative importance of SAR observables in driving AGB prediction variance [33]. Unlike traditional sensitivity measures, the Shapley effects address predictor correlation by averaging each variable's marginal contribution across all possible input orderings, conditioning on the observed joint distribution to preserve intervariable dependencies. The Shapley effect for variable $X_i$ is defined as

$$\phi_i = \sum_{S \subseteq \{1,\ldots,p\}\setminus\{i\}} \frac{|S|!\,(p-|S|-1)!}{p!}\left[V(S \cup \{i\}) - V(S)\right] \qquad (3)$$

where $p$ is the number of inputs, $S$ is a subset excluding $X_i$, and $V(S) = \mathrm{Var}(\mathbb{E}[Y \mid \mathbf{X}_S])/\mathrm{Var}(Y)$ is the closed variance function. The Shapley effects sum to unity, providing a robust variance decomposition under correlated inputs. Indices were estimated using the random permutation algorithm with $n_{\mathrm{perm}} = 100$ permutations and bootstrap confidence intervals (95%) derived from 200 resampling iterations. To identify AGB-dependent shifts in predictor importance, the analyses were stratified by AGB intervals (0–20, 20–40, 40–60, 60–80, and >80 Mg ha$^{-1}$).

## IV. Results and Discussion

### A. Model Validation and Cross-Site Performance

The validation analysis evaluates the predictive ability and bias characteristics of both algorithms under site-specific and combined calibration settings (Fig. 1). Combined calibration pools data from KNP and ILCP to derive generalized parameters. Under site-specific calibration [Fig. 1(a) and (b)], both models perform well as parameters reflect dominant scattering behavior within each ecosystem. ILCP, characterized by higher AGB woody savanna (100–140 Mg ha$^{-1}$), yields almost similar performance for the hybrid model ($R^2$ = 0.65 and RMSE = 16.63 Mg ha$^{-1}$) [Fig. 1(b)]. KNP, a lower AGB mixed woodland–savanna (20–40 Mg ha$^{-1}$), shows accurate predictions and negligible bias for both models [Fig. 1(a) and (b)]. Combined calibration, however, reveals contrasting model responses to structural heterogeneity across sites [compare Fig. 1(a) and (b) with (c) and (d)]. While both models achieve similar site-specific performance [$R^2$ $\approx$ 0.63–0.65; Fig. 1(a) and (b)], the additive saturation model [see (1)]

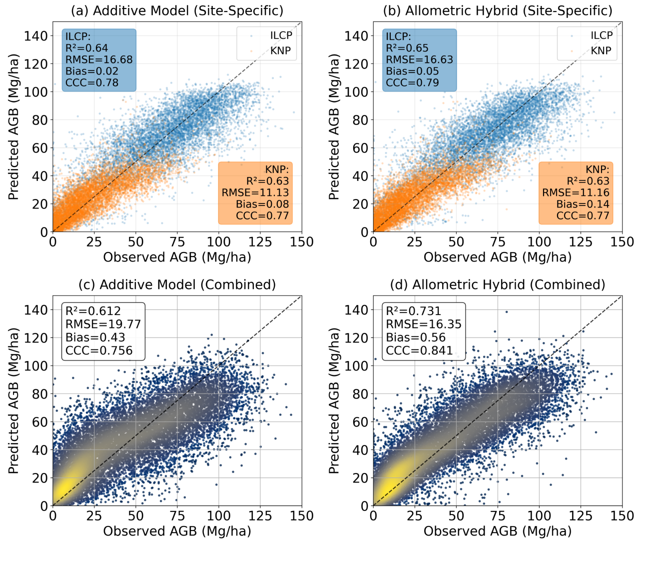


Fig. 1. Comparison of observed versus predicted AGB for different model structures and calibration approaches.

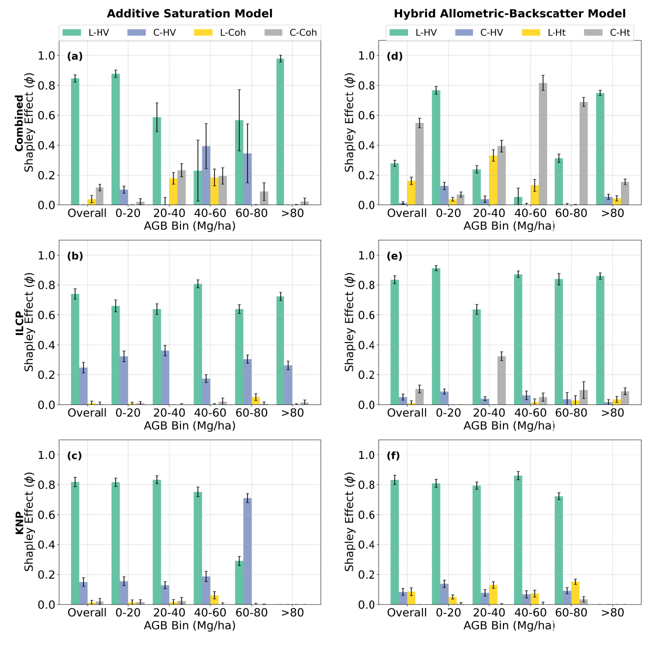


Fig. 2. Shapley effects ($\phi$) for both models across AGB classes under site-specific and combined calibration.

shows slightly reduced performance under combined calibration [$R^2$ = 0.612 and RMSE = 19.77 Mg ha$^{-1}$; Fig. 1(c)], whereas the hybrid allometric-backscatter model [see (2)] maintains strong performance [$R^2$ = 0.731 and RMSE = 16.35 Mg ha$^{-1}$; Fig. 1(d)], suggesting greater robustness to the contrasting vegetation structures of KNP and ILCP.

The hybrid model's superior generalization under combined calibration (CCC = 0.841 versus 0.756; Fig. 1) reflects the structural consistency of the height-AGB allometric relationship across the pooled gradient. Unlike backscatter and coherence, which vary with site-specific soil moisture, surface roughness, and canopy architecture, allometric height–AGB scaling follows fundamental biophysical growth principles that remain consistent across structurally diverse sites [34]. The RVoG-based inversion explicitly accounts for ground contributions and temporal decorrelation that confound direct coherence-based retrievals, enabling generalization beyond local calibration. The slightly elevated combined RMSE propagates from ILCP, where greater structural complexity increases site-specific error, while the unified backscatter term captures radiometric variations associated with woody fraction and soil dielectric properties.

### B. Sensitivity Analysis Across AGB Gradients

The Shapley effects quantified the contribution of each SAR observable to AGB prediction variance [Fig. 2(a)–(f)]. Under site-specific calibration, L-HV dominates both models at both sites [$\phi$ = 0.74–0.83; Fig. 2(b), (c), (e), and (f)]. C-band backscatter contributes moderately where canopy gaps permit penetration, peaking at 20–40 Mg ha$^{-1}$ at ILCP [$\phi$ = 0.36; Fig. 2(b)] and at 60–80 Mg ha$^{-1}$ at KNP [$\phi$ = 0.71; Fig. 2(c)]. Coherence terms contribute minimally in the additive model [$\phi < 0.05$; Fig. 2(b) and (c)], consistent with phase degradation under the 70-day ALOS-2 temporal baseline. In the hybrid model, C-band height contributes moderately at ILCP in the 20–40 Mg ha$^{-1}$ bin [$\phi$ = 0.32; Fig. 2(e)], while L-band height shows limited influence at KNP [$\phi$ = 0.15 at 60–80 Mg ha$^{-1}$; Fig. 2(f)].

Sensitivity patterns reorganize under combined calibration as models must capture scattering behavior across structurally distinct sites [Fig. 2(a) and (d)]. For the additive model, L-HV maintains overall dominance [$\phi$ = 0.85; Fig. 2(a)], with higher sensitivity at 0–20 Mg ha$^{-1}$ ($\phi$ = 0.88) and >80 Mg ha$^{-1}$ ($\phi$ = 0.98), corresponding to surface scattering at low biomass and trunk-ground interactions at high biomass. C-HV peaks at 40–60 Mg ha$^{-1}$ and 60–80 Mg ha$^{-1}$ [$\phi$ = 0.39 and $\phi$ = 0.38, respectively; Fig. 2(a)] in transitional canopy structures, while coherence remains underutilized ($\phi \leq 0.12$). The hybrid model exhibits a different sensitivity structure [Fig. 2(d)], with L-HV sensitivity decreasing at 40–80 Mg ha$^{-1}$, where height metrics become primary; C-band height peaks at 40–60 Mg ha$^{-1}$ ($\phi$ = 0.82) and 60–80 Mg ha$^{-1}$ ($\phi$ = 0.69), while L-band height contributes at 20–40 Mg ha$^{-1}$ [$\phi$ = 0.33; Fig. 2(d)]. Together, L-band backscatter remains the primary AGB predictor across ecosystems, while height metrics provide complementary sensitivity where backscatter saturates. The contribution of C-band height under combined calibration reflects both its structural sensitivity and the coherence stability preserved by the 12-day Sentinel-1 repeat cycle, while the longer ALOS-2 temporal baseline causes decorrelation, making C-band height a more reliable structural observable despite shallower penetration. The allometric height–AGB relationship follows fundamental biophysical growth principles governed by stem diameter, wood density, and architectural constraints [34], supporting the robustness of the hybrid model under pooled calibration.

## V. Conclusion

This study developed two physically based models for savanna AGB estimation using multifrequency SAR. The first, an additive saturation model, combines L- and C-band backscatter with InSAR coherence as independent exponential terms, while the second, a hybrid allometric-backscatter model, integrates RVoG-derived canopy height with unified backscatter. While both models performed comparably under site-specific calibration due to the locally fitted parameters capturing site-dependent scattering behaviors, a clear distinction emerged during combined calibration. The additive model exhibited lower predictive consistency under combined calibration, as independent saturation terms could not fully capture scattering variability across structurally distinct sites. In contrast, the hybrid model proved more robust by leveraging height integration, yielding higher explained variance and lower error under combined calibration ($R^2$ = 0.731 versus 0.612; Fig. 1). The Shapley sensitivity analysis showed that L-band HV backscatter dominated under site-specific calibration ($\phi$ = 0.74–0.83), while C-band height became the primary contributor at 40–60 Mg ha$^{-1}$ ($\phi$ = 0.82) under combined calibration, where backscatter sensitivity diminishes (Fig. 2). Although coherence currently contributes little due to temporal decorrelation from extended repeat cycles, shorter repeat cycles, such as NISAR's 12-day L-band acquisition, may improve coherence-based retrieval. More critically, RVoG-derived height provides structural information orthogonal to backscatter, though its advantage remains modest in savannas where AGB rarely exceeds L-band saturation thresholds, and requires validation in higher AGB ecosystems.

## Acknowledgment

This study was also conducted within the JAXA Kyoto and Carbon (K&C) Initiative. ALOS-2 PALSAR-2 data were provided by JAXA.

## References

[1] J. Grace, J. S. José, P. Meir, H. S. Miranda, and R. A. Montes, "Productivity and carbon fluxes of tropical savannas," *J. Biogeography*, vol. 33, no. 3, pp. 387–400, Mar. 2006.

[2] C. Tucker et al., "Sub-continental-scale carbon stocks of individual trees in African drylands," *Nature*, vol. 615, no. 7950, pp. 80–86, Mar. 2023.

[3] P. W. Ellis et al., "The principles of natural climate solutions," *Nature Commun.*, vol. 15, no. 1, p. 547, 2024.

[4] K. Wessels et al., "Quantifying the sensitivity of L-band SAR to a decade of vegetation structure changes in savannas," *Remote Sens. Environ.*, vol. 284, Jan. 2023, Art. no. 113369.

[5] X. Li et al., "First validation of GEDI canopy heights in African savannas," *Remote Sens. Environ.*, vol. 285, Feb. 2023, Art. no. 113402.

[6] R. Lucas et al., "An evaluation of the ALOS PALSAR L-band backscatter—Above ground biomass relationship Queensland, Australia: Impacts of surface moisture condition and vegetation structure," *IEEE J. Sel. Topics Appl. Earth Observ. Remote Sens.*, vol. 3, no. 4, pp. 576–593, Dec. 2010.

[7] X. Li et al., "Evaluation of GEDI footprint level biomass models in southern African savannas using airborne LiDAR and field measurements," *Sci. Remote Sens.*, vol. 10, Dec. 2024, Art. no. 100161.

[8] L. Duncanson et al., "Aboveground biomass density models for NASA's Global Ecosystem Dynamics Investigation (GEDI) LiDAR mission," *Remote Sens. Environ.*, vol. 270, Feb. 2022, Art. no. 112845.

[9] T. Bossy et al., "State of the art in remote sensing monitoring of carbon dynamics in African tropical forests," *Frontiers Remote Sens.*, vol. 6, 2025, Art. no. 1532280, doi: 10.3389/frsen.2025.1532280.

[10] M. L. Imhoff, "Radar backscatter and biomass saturation: Ramifications for global biomass inventory," *IEEE Trans. Geosci. Remote Sens.*, vol. 33, no. 2, pp. 511–518, Mar. 1995.

[11] E. S. Kasischke, M. A. Tanase, L. L. Bourgeau-Chavez, and M. Borr, "Soil moisture limitations on monitoring boreal forest regrowth using spaceborne L-band SAR data," *Remote Sens. Environ.*, vol. 115, no. 1, pp. 227–232, Jan. 2011.

[12] N. Joshi et al., "Understanding 'saturation' of radar signals over forests," *Sci. Rep.*, vol. 7, no. 1, p. 3505, Jun. 2017.

[13] C. Thiel and C. Schmullius, "The potential of ALOS PALSAR backscatter and InSAR coherence for forest growing stock volume estimation in central Siberia," *Remote Sens. Environ.*, vol. 173, pp. 258–273, Feb. 2016.

[14] A. Olesk, J. Praks, O. Antropov, K. Zalite, T. Arumäe, and K. Voormansik, "Interferometric SAR coherence models for characterization of hemiboreal forests using TanDEM-X data," *Remote Sens.*, vol. 8, no. 9, p. 700, Aug. 2016.

[15] O. Cartus, M. Santoro, U. Wegmüller, N. Labrière, and J. Chave, "Sentinel-1 coherence for mapping above-ground biomass in semiarid forest areas," *IEEE Geosci. Remote Sens. Lett.*, vol. 19, pp. 1–5, 2022.

[16] J. Askne, M. Santoro, G. Smith, and J. E. S. Fransson, "Multitemporal repeat-pass SAR interferometry of boreal forests," *IEEE Trans. Geosci. Remote Sens.*, vol. 41, no. 7, pp. 1540–1550, Jul. 2003.

[17] C. Thiel and C. Schmullius, "Impact of tree species on magnitude of PALSAR interferometric coherence over Siberian forest at frozen and unfrozen conditions," *Remote Sens.*, vol. 6, no. 2, pp. 1124–1136, Jan. 2014.

[18] Y. Lei, P. Siqueira, N. Torbick, M. Ducey, D. Chowdhury, and W. Salas, "Generation of large-scale moderate-resolution forest height mosaic with spaceborne repeat-pass SAR interferometry and LiDAR," *IEEE Trans. Geosci. Remote Sens.*, vol. 57, no. 2, pp. 770–787, Feb. 2019.

[19] N. Bhogapurapu, P. Siqueira, J. Armston, M. Urbazaev, K. Wessels, and L. Duncanson, "Canopy height estimation using C- and L-band InSAR coherence over savannas and dry forests," in *Proc. IEEE Int. Geosci. Remote Sens. Symp.*, Jul. 2024, pp. 2290–2293.

[20] N. Ghasemi, V. Tolpekin, and A. Stein, "Assessment of forest above-ground biomass estimation from PolInSAR in the presence of temporal decorrelation," *Remote Sens.*, vol. 10, no. 6, p. 815, May 2018.

[21] M. Santoro and O. Cartus, "Research pathways of forest above-ground biomass estimation based on SAR backscatter and interferometric SAR observations," *Remote Sens.*, vol. 10, no. 4, p. 608, Apr. 2018.

[22] M. Neumann, S. S. Saatchi, L. M. H. Ulander, and J. E. S. Fransson, "Assessing performance of L- and P-band polarimetric interferometric SAR data in estimating boreal forest above-ground biomass," *IEEE Trans. Geosci. Remote Sens.*, vol. 50, no. 3, pp. 714–726, Mar. 2012.

[23] A. Bouvet et al., "An above-ground biomass map of African savannahs and woodlands at 25 m resolution derived from ALOS PALSAR," *Remote Sens. Environ.*, vol. 206, pp. 156–173, Mar. 2018.

[24] K. J. Wessels et al., "Assessing the impacts of changing elephant densities on woody vegetation structure in private reserves within the Greater Kruger National Park, South Africa," *Biol. Conservation*, vol. 317, May 2026, Art. no. 111815.

[25] D. M. Olson et al., "Terrestrial ecoregions of the world: A new map of life on Earth," *BioScience*, vol. 51, no. 11, pp. 933–938, 2001.

[26] E. Dinerstein et al., "An ecoregion-based approach to protecting half the terrestrial realm," *BioScience*, vol. 67, no. 6, pp. 534–545, Jun. 2017.

[27] M. S. Colgan, G. P. Asner, and T. Swemmer, "Harvesting tree biomass at the stand level to assess the accuracy of field and airborne biomass estimation in savannas," *Ecolog. Appl.*, vol. 23, no. 5, pp. 1170–1184, Jul. 2013.

[28] K. I. Paul et al., "Testing the generality of above-ground biomass allometry across plant functional types at the continent scale," *Global Change Biol.*, vol. 22, no. 6, pp. 2106–2124, 2016.

[29] J. R. Kellner, J. Armston, and L. Duncanson, "Algorithm theoretical basis document for GEDI footprint aboveground biomass density," *Earth Space Sci.*, vol. 10, no. 4, p. 2022, Apr. 2023.

[30] X. Huang, B. Ziniti, N. Torbick, and M. J. Ducey, "Assessment of forest above ground biomass estimation using multi-temporal C-band Sentinel-1 and polarimetric L-band PALSAR-2 data," *Remote Sens.*, vol. 10, no. 9, p. 1424, Sep. 2018.

[31] R. M. Lucas, M. Moghaddam, and N. Cronin, "Microwave scattering from mixed-species forests, Queensland, Australia," *IEEE Trans. Geosci. Remote Sens.*, vol. 42, no. 10, pp. 2142–2159, Oct. 2004.

[32] S. Zwieback, S. Hensley, and I. Hajnsek, "Assessment of soil moisture effects on L-band radar interferometry," *Remote Sens. Environ.*, vol. 164, pp. 77–89, Jul. 2015.

[33] E. Song, B. L. Nelson, and J. Staum, "Shapley effects for global sensitivity analysis: Theory and computation," *SIAM/ASA J. Uncertainty Quantification*, vol. 4, no. 1, pp. 1060–1083, Jan. 2016.

[34] T. R. Feldpausch et al., "Tree height integrated into pantropical forest biomass estimates," *Biogeosciences*, vol. 9, no. 8, pp. 3381–3403, 2012.